Materials Science in Semiconductor Processing 206 (2026) 110428

Contents lists available at ScienceDirect

Materials Science in Semiconductor Processing

journal homepage: www.elsevier.com/locate/mssp

How the absorber thickness affects the electrical and structural properties of Sb_2Se_3 solar cells

N. Torabi [a], J.M. Delgado-Sanchez [b], E. Artegiani [a], J. Kuliček [c], B. Rezek [c], P. Jakuza [d], M. Meneghini [d], A. Romeo [a,*]

[a] LAPS-Laboratory for Photovoltaics and Solid-State Physics, Department of Computer Science, University of Verona, Ca' Vignal 1, Strada Le Grazie 15, 37134, Verona, Italy
[b] Department of Applied Physics, University of Seville, Ctra. Utrera km 1, 41013, Seville, Spain
[c] Faculty of Electrical Engineering, Czech Technical University in Prague, Technická 2, 6, Prague, Czechia
[d] Department of Information Engineering, University of Padova, via Gradenigo 6/B, 35131, Padova, Italy

ARTICLE INFO

Keywords:
Sb_2Se_3 solar cells
Post-annealing treatment
Absorber thickness
Thin film solar cells

ABSTRACT

This work investigates how the absorber thickness and a mild post-annealing treatment (PAT) in air jointly affect the structural and electrical properties of thermally evaporated Sb_2Se_3 absorbers, and the performance of superstrate solar cells. Sb_2Se_3 layers with thicknesses of 400, 800, and 1200 nm were deposited on a CdSe buffer and integrated in glass/SnO_2:F/SnO_2/CdSe/Sb_2Se_3/Au devices. Contrary to the usual expectation for thin-film absorbers, the thinnest device (400 nm) yields the highest power conversion efficiency (PCE), increasing from 2.8 % to 3.7 % after annealing in air, while thicker absorbers (800 and 1200 nm) only reach 3.5 % and 3.3 %, respectively. These trends correlate with a higher hole concentration ($\approx 4.6 \times 10^{16}$ cm^{-3} before PAT and $\approx 1.3 \times 10^{17}$ cm^{-3} after PAT) and reduced defect density in the thinnest absorber, as revealed by CV/DLCP analysis, which also shows a narrowing of the space-charge region that favors carrier collection in ultra-thin devices.

Morphological and XRD analyses confirm conventional grain growth and only subtle changes in crystal orientation with thickness and annealing, indicating that microstructural evolution alone does not govern the efficiency trends. Instead, SIMS profiles show oxygen incorporation throughout the absorber after PAT, while PL measurements and the convergence of CV and DLCP profiles demonstrate suppression of deep defects. These observations point to oxygen-induced passivation of electrically active defects as the main mechanism behind the improved open-circuit voltage and fill factor. Overall, the results highlight that in Sb_2Se_3/CdSe solar cells with very high absorption coefficients, carrier transport, defect passivation, and space-charge region engineering are more critical than increasing the absorber thickness, enabling efficient devices with ultra-thin (400 nm) Sb_2Se_3 absorbers.

1. Introduction

Sb_2Se_3 is a semiconductor composed of earth-abundant and low-toxic elements, possessing an optimal band gap of around 1–1.2 eV [1]. Its high optical absorption coefficient ($>10^5$ cm^{-1}) allows it to capture all photons using a very thin layer (within 800 nm thickness) [2]. These features make Sb_2Se_3 a good choice for lightweight opto-electronic applications with low-cost fabrication processes. Moreover, its quasi-one-dimensional (Q-1D) crystal structure makes Sb_2Se_3 particularly interesting for photovoltaic applications. While grain boundaries of polycrystalline solar cells are defect sites, leading to charge recombination, the Q-1D structure of Sb_2Se_3 can mitigate this issue through anisotropic charge transportation [3]. A decade of investigation into Sb_2Se_3 thin film solar cells has yielded a power conversion efficiency (PCE) up to 10 % [4,5].

In some recent papers the absorber thickness is related to the Sb_2Se_3 solar cell efficiency. The carrier transport was shown to be highly thickness-dependent in Sb_2Se_3 solar cells with an n-i-p structure, and an absorber thickness of 550 nm was found to be optimal for enhancing the extraction of photogenerated carriers [6]. Another study, on $Sb_2(S,Se)_3$ solar cells, showed that increasing the absorber thickness from 95 nm to 210 nm reduces the Urbach energy and the defect states, increasing the

---

* Corresponding author.
E-mail address: alessandro.romeo@univr.it (A. Romeo).

https://doi.org/10.1016/j.mssp.2026.110428
Received 13 November 2025; Received in revised form 15 December 2025; Accepted 6 January 2026

efficiency [7]. In this work Sb_2Se_3 based solar cells with three different absorber thicknesses are analyzed and compared, it was found out that the relation between efficiency and thickness is different from other thin film solar cells [8,9]. Also, we have studied the effect of oxygen on differently thick Sb_2Se_3 absorbers. Various annealing processes have been reported to be beneficial for Sb_2Se_3 thin film solar cells, such as annealing in vacuum [10], in Se [11], in H_2S [12] ambient and by $MgCl_2$ treatment [13]. It has also been observed that simple air exposure at room temperature, under atmospheric pressure, results in the formation of a few nanometers-thick Sb_2O_3 layer on the Sb_2Se_3 surface, which improves hole extraction by acting as an interface barrier [14]. Ren et al. showed that careful oxide management at the Sb_2Se_3/Al interface allows the use aluminum as a back contact by enhancing hole extraction [15]. Since oxygen seems to have an important role, also the effect of oxidation on the absorber thickness can have a role. In our work, we observe that a post-deposition annealing treatment (PAT) is having a different influence based on absorber thickness.

In our laboratory, we grow Sb_2Se_3 at a low substrate temperature using a thermal evaporation method. One of the key advantages of this technique is the possibility to have a fine control of the deposition rate and, correspondingly, of the absorber thickness. So Sb_2Se_3 films with 400, 800, and 1200 nm thicknesses have been deposited in superstrate configuration. The solar cells are fabricated and studied in a glass/SnO_2:F/SnO_2/CdSe/Sb_2Se_3/Au structure. CdSe was previously studied by the same authors as an alternative buffer layer to the commonly used CdS, which enhances both J_{sc} and the stability of the devices [16], so it is now part of our standard solar cell structure. In this direction it has been shown that the presence of Se prior to Sb_2Se_3 deposition is a way to reduce Se vacancies [17]. An annealing in air -PAT-was applied to the finished devices, with an optimized annealing temperature and time respectively 150 °C and 20 min.

2. Methods

2.1. Device fabrication

Commercial coated SnO_2:F/SnO_2 glasses (NSG TEC 12D) are used as substrates, where a 100 nm thick CdSe buffer layer is thermally evaporated at 340 °C under a pressure of $1*10^{-4}$ Pa. As extensively discussed in one of our previous papers, we chose CdSe instead of the most conventional CdS to avoid sulphur diffusion [18]. After window layer deposition, Sb_2Se_3 is grown at a substrate temperature of 300 °C by evaporation of Sb_2Se_3 lumps from a graphite crucible at 500–600 °C and under a pressure of $2*10^{-4}$ Pa, obtaining an evaporation rate of 0.15 nm/s. Then we apply a vacuum annealing step, which is carried out in the same chamber at 350 °C for 30 min. The back contact -a simple 30 nm thick gold layer-is thermally evaporated (forming a cell area of 0.13 cm^2) on top of the absorber. The devices are labelled T400, T800, and T1200 according to their absorber thickness (400 nm, 800 nm and 1200 nm). Some devices are submitted to the above mentioned PAT in a muffle furnace at a temperature of 150 °C for 20 min, these will be called T400-PAT, T800-PAT, and T1200-PAT. Performing post-annealing in air arose from our experimental observation that simply keeping Sb_2Se_3 films in atmosphere for several days led to a clear improvement in the device performance, with a reduction of the rollover effect in the J–V characteristics. This behavior suggested that a mild oxidation could have a beneficial passivating effect, as also reported in the introduction.

In order of being able to systematically reproduce and control the phenomenon, we initially performed a series of annealing tests varying the temperature from 100 °C to 170 °C (see Fig. S1 and table TS1 in supplementary materials) and the duration from 5 to 45 min (see Fig. S2 and table TS2 in supplementary materials).

The condition of 150 °C for 20 min yielded the most reproducible improvement.

2.2. Characterization techniques

X-ray diffraction (XRD) was carried out with a Rigaku diffractometer system with a PhetenMax high-flux 9 kW rotating anode X-ray source, coupled with an XSPA-400ER 2D/1D/0D hybrid pixel array direct photon counting detector. The morphology and elemental composition of the crystalline phases were analyzed by scanning electron microscopy (SEM/EDX), using a JEOL microscope (JSM 5400 Model) and operating at 20 kV. This equipment is connected to an energy dispersive system X-ray (EDX) (Oxford Link ISIS), which allows chemical analysis of samples using a detector of Si/Li with a Be window. Depth profiles were obtained by Secondary Ion Mass Spectrometry (SIMS) using a CAMECA IMS-4f instrument with a Cs^+ primary ion beam at a 10 kV accelerating voltage (corresponding to 5.5 keV impact energy) for the detection of positive secondary ions. Finished cells have been analyzed by means of current density-voltage (JV), capacitance-voltage (CV) and external quantum efficiency (EQE). JV characteristics were collected with a Keithley Source Meter 2420, under an AM 1.5 spectrum at 100 mW/cm^2, using a LOT Quantum Design Europe solar simulator LS0306. EQE spectra were acquired using a commercial LOANA solar cell analysis system, calibrated with a silicon reference sample with known EQE using an incident spotlight of 1 mm × 2 mm area. CV and drive level capacitance profiling (DLCP) were conducted using an HP4284A LCR meter, controlled by a specific in-house software. The PL spectra on CdSe/Sb_2Se_3 solar cells were obtained using a confocal photoluminescence microscope (WITec alpha300 RAS) equipped with a tunable laser (NKT Photonics, excitation wavelength 500 nm, laser power 200 μW). PL spectra were collected by 100 × objective (NA 0.9) and UHTS 300 VIS spectrometer. The integration time was 240 s, with a number of accumulations of 2. Spectra were collected and processed by WITec Control 6.1 and WITec Project 6.1 software.

3. Results and discussion

3.1. Performance of the solar cells

In Fig. 1 the JV characteristics are shown, these -together with the resulting photovoltaic parameters of the best-performing devices (see Table 1)- show that the thinner absorber cell (T400) delivers the highest efficiency. Although the thicker absorbers are expected to improve light absorption and the crystalline quality, the lower J_{sc} values indicate a limitation in carrier collection efficiency.

This, despite the increased thickness, highlights the carrier transport rather than the light absorption as a more limiting factor. Obviously, it could be attributed to the longer travel path of the photo-generated carriers, giving way to more recombination, corroborated by the higher fill factor of the T400 cell. By increasing the absorber thickness, a

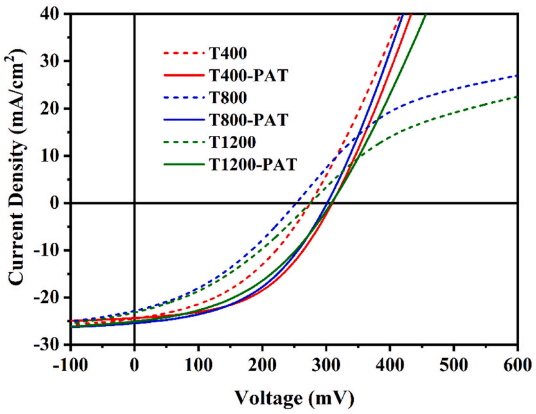

Fig. 1. Current-voltage curves of solar cells with different absorber thicknesses before and after PAT.

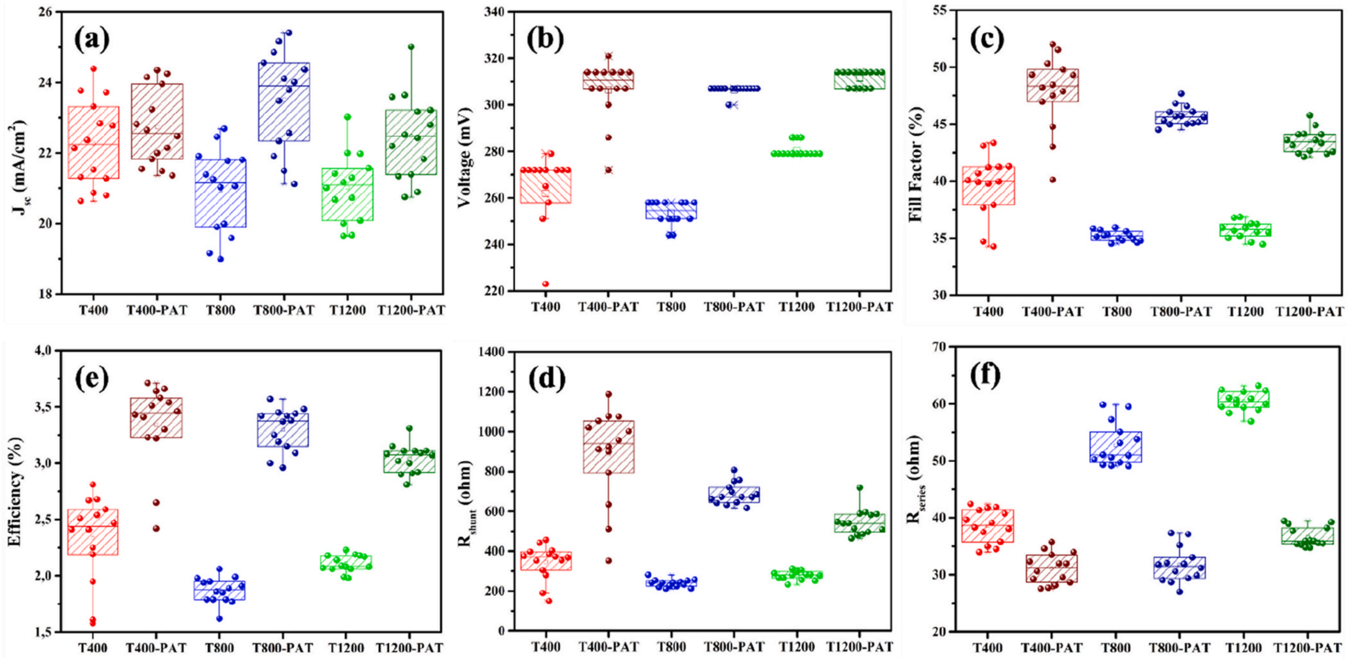

Fig. 2. Box plots of photovoltaic parameters of twelve Sb_2Se_3 solar cells with different absorber thicknesses before and after PAT.

Table 1

Photovoltaic parameters of best-performing Sb_2Se_3 solar cells with different absorber thickness before and after PAT. Statistical data are presented in Fig. 2.

Sample	J_{sc} (mA/cm^2)	V_{oc} (mV)	FF (%)	η (%)	R_{shunt} (Ω)	R_{series} (Ω)
T400	24.3	279	41	2.8	384	35
T800	22.6	258	35	2.0	232	49
T1200	23.0	279	35	2.2	232	57
T400-PAT	24.3	314	48	3.7	924	30
T800-PAT	25.4	307	46	3.5	632	29
T1200-PAT	25.0	314	42	3.3	486	36

strong rollover appears in the JV characteristics, together with an increase in the series resistance; meanwhile the shunt resistance is reduced, leading to a decrease in the fill factor for higher thicknesses. At the same time all the samples show comparable V_{oc} values.

After PAT, the efficiency in all cases increases by more than 1 % (the values are reported in Table 1). This annealing leads to a decrease in the series resistance and a corresponding increase in the shunt resistance, especially for thicker samples, where the rollover in the JVs vanishes. PAT improves the V_{oc} and FF of all cases and increases the J_{sc} of the thicker absorber cells (T800 and T1200). For the T400 cell, after PAT, we register the highest efficiency; this is due to a higher FF and shunt resistance compared to the thicker samples, while J_{sc} remains practically the same.

To give more consistency to these observations, we show -in Fig. 2- the statistical distribution of photovoltaic parameters of 12 different cells, which confirms the above-described behavior. The improvement of all parameters after PAT, as well as the overall better performance of 400 nm thick Sb_2Se_3 devices, is consistently observed. A significant improvement in V_{oc} and FF is registered for all the devices, while T800 and T1200 also show the vanishing of the rollover effect and a more substantial J_{sc} increase.

The disappearance of the rollover effect in the JV characteristics after PAT could be attributed to several causes. One plausible explanation is the improved passivation of interface and surface defects, which reduces recombination centers that hinder charge extraction near the absorber/contact interfaces.

3.2. *Structural properties*

Scanning electron microscope images of the Sb_2Se_3 films with different thickness show a very slight increase of the grains as the film thickness increases (Fig. 3a, c, and 3e), since the average grain size evolves from 200 nm to 300 nm. This is typical for thin film materials, where the grain size generally scales with thickness, potentially improving the device performance by reducing the grain boundary density. So, a higher performance would be expected for the 1200 nm-thick Sb_2Se_3 absorber, but this was not observed.

In addition to grain size and the associated surface recombination, several other parameters influence the performance of Sb_2Se_3 solar cells as the absorber thickness increases. One critical factor is the rise in bulk recombination, as the thickness increases the distance that photo-generated carriers must travel before collection, raising the likelihood of recombination losses. Moreover, thicker absorbers can lead to a less favorable electric field distribution, which limits an efficient carrier separation. These issues will be analysed in the next sections through electrical measurements (CV and DLCP analysis).

After PAT (Fig. 3b, d, and 3f), only minor morphological changes are observed. Additionally, surface aggregations emerge, particularly in the thicker films. In the T800-PAT sample, a needle-shaped structure appears, while the T1200-PAT sample exhibits particle-like features. These formations are most likely needle-shaped crystallites embedded within the larger grains.

Considering the low annealing temperature, this white stripes' contrast is likely due to pre-existing crystallographic features that become electronically distinct after mild air annealing due to a partial oxidation or a relaxation of internal strain. As a matter of fact, these features exhibit a higher electron emission (appearing with a brighter contrast in SEM images). This behavior could be explained by an overall surface oxidation, potentially induced by the air annealing process at 150 °C, bringing out these stripes by slight work function variations (Sb_2O_3 vs Sb_2Se_3).

Considering the ribbon-like structure of Sb_2Se_3, as mentioned before, and the extremely small diameters of the observed needles (about 15 nm in size), we can assume them to be an aggregation of ribbons that take part in the composition of the single grains.

The facets with highly tilted ribbons with respect to the substrate

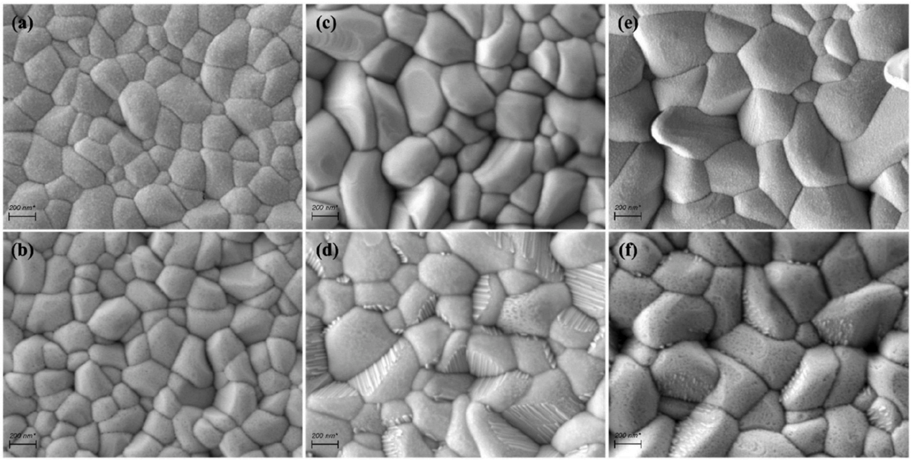

Fig. 3. Top-view SEM images of (a) T400, (b) T400-PAT, (c) T800, (d) T800-PAT, (e) T1200, and (f) T1200-PAT Sb_2Se_3 films.

exhibit a larger area exposed to air, and so they show a larger number of needle-like features.

This could give an information on the orientation of the different ribbons, in this sense the 400 nm absorber samples would show ribbons that seem orthogonal, whereas the 800 nm case and the 1200 nm films show more tilted ribbons, where the 1200 nm sample displays more embedded tips compared to the 800 nm case. This suggests a greater accuracy in defining the orientation of the ribbons compared to the conventional texture coefficient analysis, where a large variety of different orientations are mixed in an average value.

However, this effect is also strongly influenced by the expected roughness increase with increasing thickness, which reduces the compactness of the morphology, limiting the accuracy of this observation.

Due to the small size and low thickness of these aggregations, their precise composition is difficult to detect using energy-dispersive X-ray. Also, Raman spectroscopy was not helpful in this sense (not shown here). However, their potential nature can be partially supported by the work done by Fleck et al. [14], who reported the formation of α-Sb_2O_3 on the surface through simple air exposure or air annealing.

X-ray diffraction (XRD) patterns of all Sb_2Se_3 thin film samples confirm the orthorhombic crystal structure (JCPDS No. 15–0861) of Sb_2Se_3 (Fig. 4a). The crystal structure belongs to the orthorhombic space group Pbnm, which is an alternative setting of the standard space group Pnma (No. 62).

To evaluate the preferential orientation of the crystallites, the texture coefficient (TC) of the main diffraction reflections (presented in Fig. 4b) has been calculated using the equation:

$$\mathrm{TC_{hkl}} = \frac{I_{hkl}}{I_{0\ hkl}} \Bigg/ \left(\frac{1}{N} \sum\nolimits_{N} \frac{I_{hkl}}{I_{0\ hkl}} \right)$$

Where I_{hkl} and $I_{0\ hkl}$ represent the observed intensity of the [hkl] reflections and the corresponding intensity in the standard XRD pattern, respectively. N is the number of reflections considered in the calculation. A TC value larger than one indicates a preferential orientation of the crystallites along that specific direction. The Q-1D crystal structure of Sb_2Se_3 consists of Sb-Se-Sb building blocks covalently bonded along one direction, while the interactions between these ribbons are weak van der Waals forces. Therefore, charge transport is favored when the ribbons are oriented perpendicular to the substrate -[001] direction-, while it is hindered when the ribbon orientation approaches a position parallel to the substrate (see Fig. 5).

In general, the films exhibit orientation along [hk1], with a notable texture along [021] and [041], which have a smaller angle to the substrate surface compared to the [211] and [221] directions (see Fig. 5). As the film thickness increases, an enhanced texture along the mostly desired [221] and [002] orientation is observed, together with a slight reduction of less favorable [321] and [041] orientations; however, this does not correspond to a trend in higher performance in our samples.

The crystal orientation after PAT does not exhibit a noticeable change. As shown in Fig. 6, the XRD patterns of the annealed samples are very similar to the as-deposited layers. There is just a slight change in texture coefficient values, with a slight enhancement of orientations closer to the substrate normal, such as [021], [221], [211], and [002]. However, the 400 nm film shows increased TC values for the less

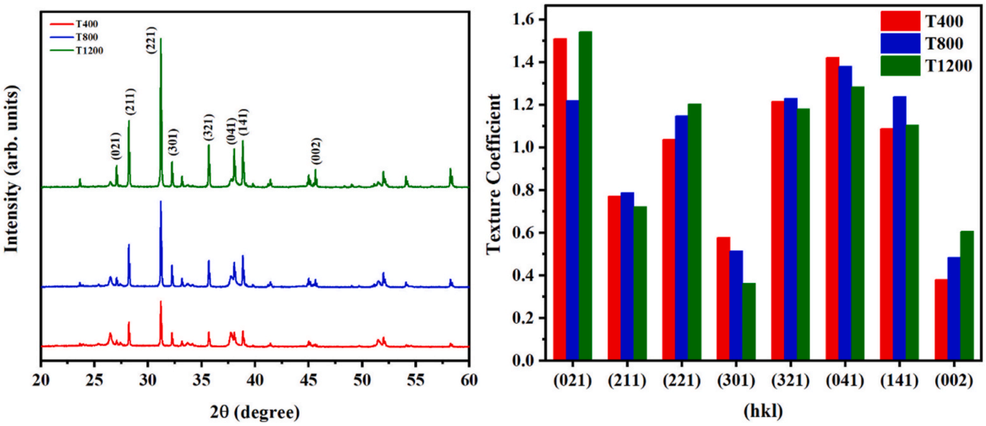

Fig. 4. (a) XRD peaks and (b) texture coefficient of $CdSe/Sb_2Se_3$ solar cells with varying absorber thickness.

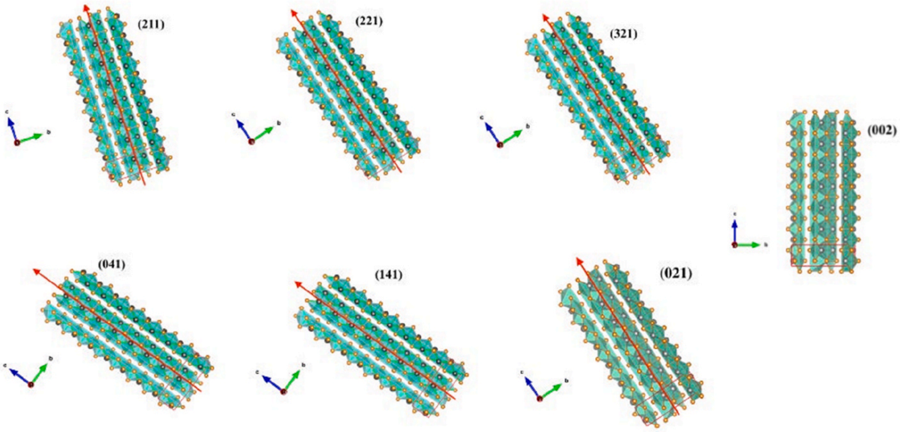

Fig. 5. Ribbon orientation and identified XRD peaks made with Vesta software [19].

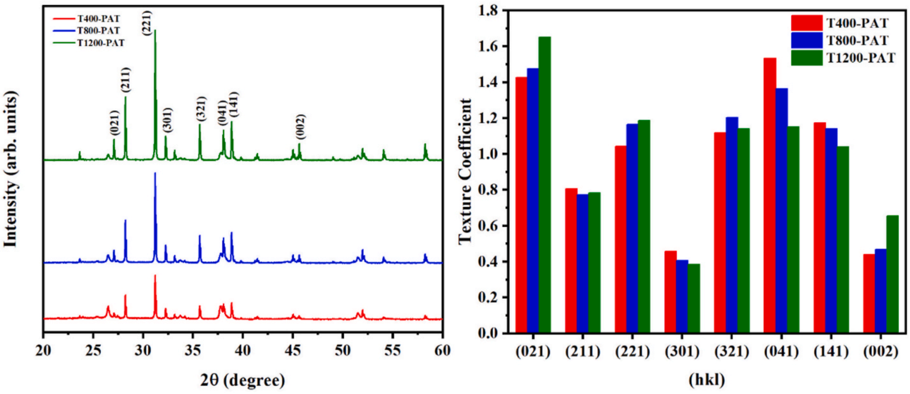

Fig. 6. (a) XRD peaks and (b) texture coefficient of CdSe/Sb_2Se_3 solar cells with varying absorber thickness after PAT.

favorable [041] and [321] orientations. Therefore, we cannot conclude any correlation between the thickness, as well as the annealing, and the orientation of the Sb_2Se_3 ribbons.

A better understanding of the PAT effects is given by SIMS analysis, which was performed on all the three different thicknesses, before and after PAT treatment. In this case, selenium has been taken as a reference element: different elements have varying secondary ion yields in SIMS analysis; thus, a known element can be used as a reference for comparison. EDX results confirm a well-defined Sb:Se stoichiometric ratio of 2:3 in all cases, indicating that a different thickness or PAT do not significantly alter the overall elemental composition of the absorber layer (not shown here). Fig. 7 shows the O/Se ratio constant throughout the absorber, demonstrating that oxygen incorporation is not limited to the surface but extends into the bulk of the material. Also, it changes according to the absorber thickness and to the annealing: for the 400 nm film, a higher oxygen content is observed throughout the layer after PAT.

3.3. Electrical properties

The external quantum efficiency (EQE) spectra show a clear difference in the electrical behavior of devices with different absorber thicknesses (shown in Fig. 8), with a higher generation/collection of carriers for the thinner case. The higher EQE response is coherent with the higher average current density measured in the JV characteristics, as shown in Fig. 1. The bandgap remains consistent across all samples, indicating that differences in EQE arise from carrier collection efficiency rather than optical absorption edge shifts. In the long wavelength region, T400 and T1200 show a similar response, indicating that the deposition of a thicker absorber does not lead to any gain in charge collection. On the other hand, the higher quantum efficiency of T400 across all wavelengths suggests a lower carrier recombination. After PAT, the 1200 nm thick sample shows EQE gain at all wavelengths, indicating reduced recombination of the carriers generated over the entire absorber width. For the thinner sample, we observe a gain between 300 and 750 nm, while the quantum efficiency reduces at long wavelengths; this is clearly addressed with the CV and DLCP analysis (see next section). The J_{sc} values calculated from EQE are consistent with those obtained from JV measurements. Although the EQE of T400 shows a slight decrease at longer wavelengths after PAT, the calculated current densities are consistent with the slightly higher current density observed in the statistics (see Fig. 2); this can be explained by the lower solar irradiation at wavelengths above 800 nm in the AM1.5 spectrum. The trend of EQE increase, especially at short wavelengths, suggests a decrease in carrier recombination in the bulk, consistent with a passivation effect of the defects through the annealing treatment in air.

CV/DLCP analysis is presented in Fig. 9. The doping concentration in the space charge region (SCR) of T400, T800, and T1200 cells is around 4.6×10^{16} cm^{-3}, 2.6×10^{16} cm^{-3}, and 2.2×10^{16} cm^{-3}, respectively. The 400 nm thick Sb_2Se_3 shows the highest doping density and, consequently, the smallest SCR width (indicated by arrows, corresponding to measurements done with a 0V bias in DC). This enhanced doping level in the thinnest device may contribute to better charge collection. In fact, for ultra-thin absorbers, one of the main issues is that the depletion layer could extend throughout the device near the back contact [9]. In this case, instead, the depletion region is restrained thanks to the high carrier concentration; this, together with the exceptionally high absorption coefficient, allows for good performance with small thicknesses, thus

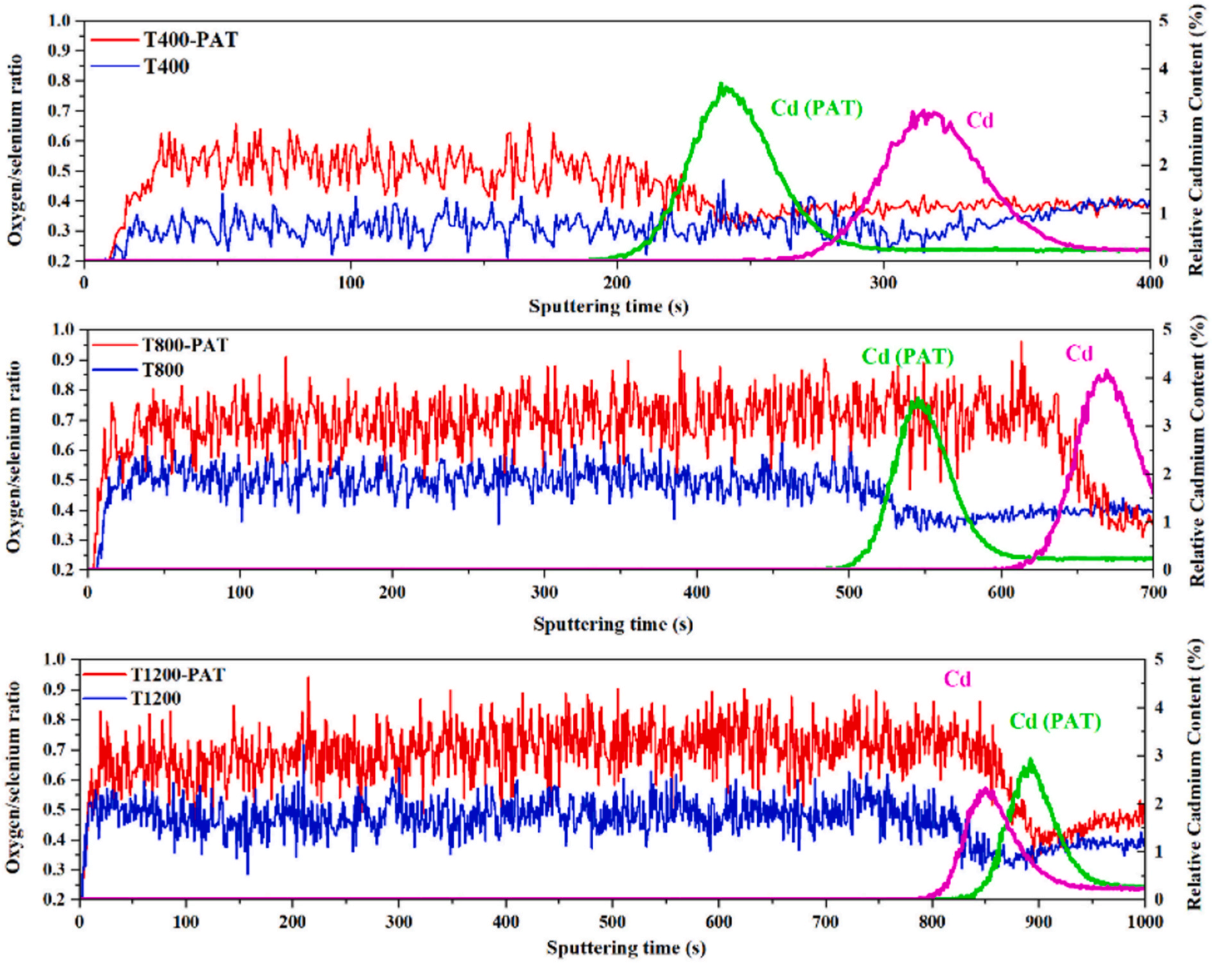

Fig. 7. SIMS analysis of the O/Se ratio of the three different devices (from top to bottom, 400, 800, and 1200 nm), before (blue line) and after (red line) PAT.

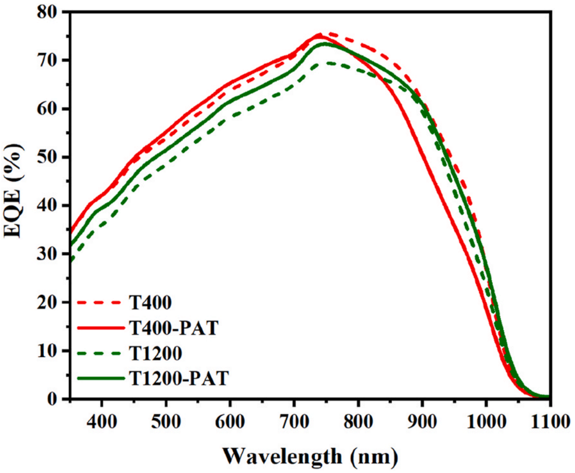

Fig. 8. EQE responses of T400 and T1200 solar cells before and after PAT.

reducing the impact of a small mean free path. On the other hand, the enhancement of the carrier concentration after PAT also explains the loss in the long-wavelength region registered in EQE after PAT. In fact, the 400 nm thick absorber exhibits a depletion layer shrinkage of about 60 nm, which further increases the distance of the active electric field from the back-end region, increasing the possibility of carrier collection loss. While the thicker absorbers show a much less significant change in the width of the depletion region after PAT.

The comparison between DLCP and CV allows for the quantification of the density of deep and shallow defects. While CV depends on both deep and shallow defects, DLCP is mainly affected by the shallow ones [19]. The difference between CV and DLCP profiles in the samples before PAT confirms the presence of deep defects (Fig. 9a). After applying PAT, the doping density increases significantly for all thicknesses, reaching values of 1.3×10^{17} cm^{-3}, 5.8×10^{16} cm^{-3}, and 3.1×10^{16} cm^{-3}, for T400-PAT, T800-PAT, and T1200-PAT, respectively. This results in a narrower space charge region width. Most notably, the CV and DLCP profiles are almost superposed after PAT, meaning effective passivation of deep traps.

These data, together with the SIMS analysis discussed in section 3.2, suggest that oxygen introduced during PAT plays a significant role in passivating electrically active defects within the Sb_2Se_3 absorber layer. Density functional theory calculations indicated that oxygen could passivate Se vacancies, shifting from deep recombination-active levels to shallow, inactive states [20].

To further investigate this effect, PL analysis has been performed on 400-nm and 1200-nm thick absorbers before and after PAT (Fig. 10). For all samples, deconvolution of the photoluminescence response has revealed the presence of three distinct peaks. The largest one (around 1.31 eV) is easily attributable to the direct band-gap transition. These PL emissions were determined as the average of 22500 spectra recorded within the 930–1020 nm spectral window, after subtraction of background contributions. These spectra represent relative PL intensity, not absolute zero-level emission, and minor shifts with respect to the nominal 1–1.2 eV bandgap are commonly observed. The nature of the other two peaks, corresponding to values of 1.26 eV and 1.22 eV, is

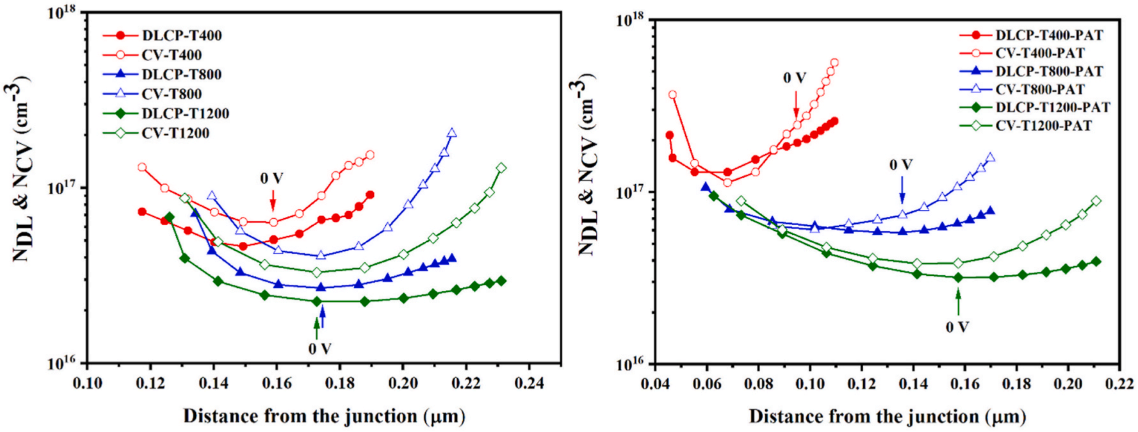

Fig. 9. Capacitance-voltage (CV) and deep-level capacitance profiling (DLCP) of different thick Sb_2Se_3 solar cells (a) before and (b) after PAT.

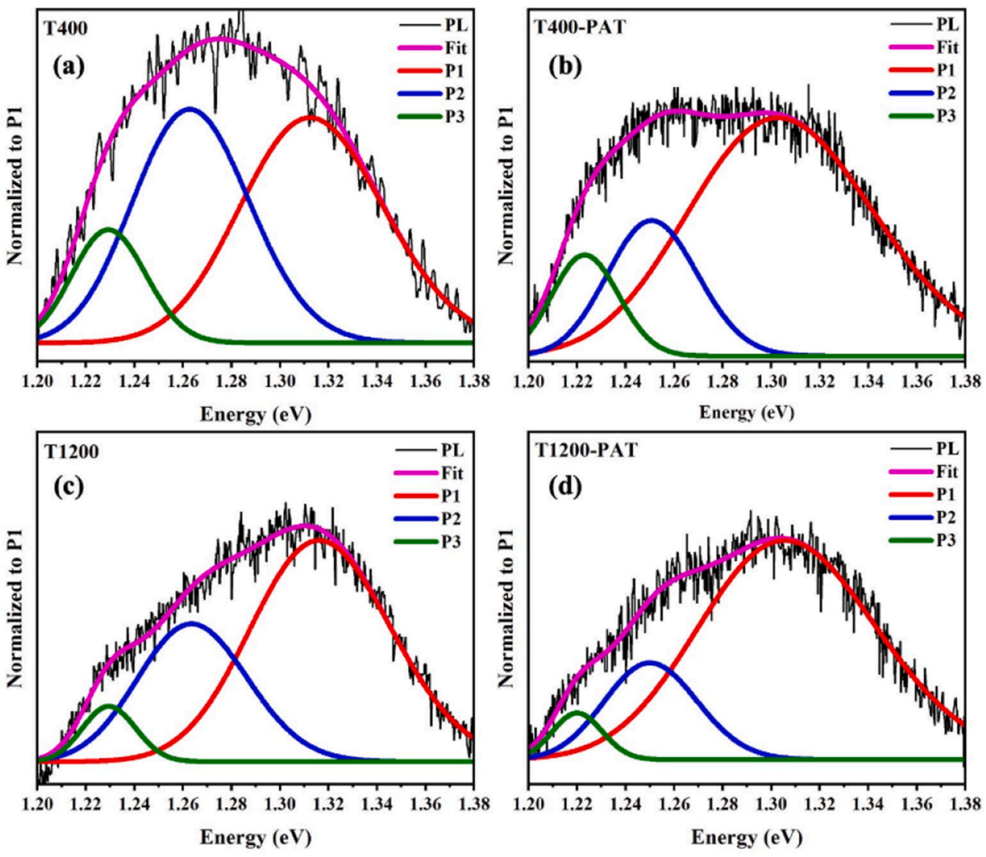

Fig. 10. PL peak intensities (normalized to P1) vs energy of (a) T400, (b) T400-PAT, (c) T1200, and (d) T1200-PAT solar cells.

summarized in Table 2. The intensity of these defect-related peaks varies between the two thicknesses.

For a straightforward comparison, the peaks have been normalized to the 1.31 eV peak of direct bandgap emission. By comparing the figures on the right with those on the left (see Fig. 10), it can be noted that the relative intensities of the two lower-energy peaks at 1.26 eV and 1.22 eV decrease significantly after PAT. This attenuation indicates a substantial reduction of defect-related radiative recombination channels, confirming the passivation effect of oxygen introduced during the annealing process. These observations are consistent with the CV/DLCP analyses, which also revealed a decrease in deep defect density after PAT.

Table 2
Observed PL peaks and proposed origins in Sb_2Se_3 solar cells.

PL Peak	Possible Origin
1.31 eV	Direct bandgap emission (near band edge)
1.26 eV	Shallow defect-related transitions
1.22 eV	Deeper defects or bound exciton emission

Finally, the stability of the finished devices has been evaluated through an accelerated lifetime test by keeping the solar cells in a specific metal box, where a rack of halogen lamps and a temperature system control allow the cells to be exposed to an illumination of one sun and a temperature of 80 °C. The devices have been measured subsequently at different aging intervals up to 200 h, and the photovoltaic parameters are presented in Fig. 11. Notably, all devices show an initial increase in performance during the first 10 h of stress, followed by a stable behavior over time. By comparing T400, T800, and T1200 solar cells, we observe an improvement in all parameters up to 100 h. As we can see, there is a large gap between the dashed and solid lines (devices with PAT), due to a stronger initial increase in efficiency parameters for cells without PAT, especially for the thicker absorber layers. The light soaking is thus more effective for the as-deposited devices. This corroborates the effect of mild oxidation in improving the performance of Sb_2Se_3 solar cells. Finally, if the photovoltaic parameters of T400-PAT and T800-PAT increase, they slightly drop in the T1200-PAT case, indicating that excessive absorber thickness may limit the stability of the devices.

4. Conclusion

The influence of Sb_2Se_3 absorber thickness and post-annealing in air (PAT) on the performance of thermally evaporated superstrate devices has been systematically evaluated by combining electrical, structural, and optical characterization. Devices with 400, 800, and 1200 nm-thick absorbers show that the thinnest configuration provides the highest efficiency, despite the nominal advantage of thicker layers for light harvesting. Before PAT, the 400 nm device already outperforms thicker cells, reaching 2.8 % efficiency versus 2.0–2.2 % for 800–1200 nm. After PAT at 150 °C for 20 min in air, the PCE further increases to 3.7 % for 400 nm, while 800 and 1200 nm devices reach 3.5 % and 3.3 %, respectively. These improvements are mainly driven by an increase in open-circuit voltage and fill factor, together with the suppression of rollover and a significant reduction in series resistance in thicker cells. CV/DLCP analysis reveals that the 400 nm absorber exhibits the highest carrier concentration ($\approx 4.6 \times 10^{16}$ cm^{-3}, rising to $\approx 1.3 \times 10^{17}$ cm^{-3} after PAT) and the narrowest depletion width, which promote efficient carrier collection even in ultra-thin films with very short transport paths. The comparison between CV and DLCP profiles shows a substantial difference before PAT, indicating the presence of deep defect states. After PAT, these profiles nearly overlap for all cases, demonstrating an effective passivation of deep traps and a concurrent increase in carrier concentration. PL measurements corroborate this picture by showing a pronounced reduction of defect-related emission peaks at 1.26 eV and 1.22 eV after annealing. SIMS depth profiles confirm that oxygen penetrates throughout the absorber, especially in thinner films. Taken together, these results point to oxygen-assisted passivation of electrically active defects (such as Se vacancies), which reduces recombination, enhances band-edge emission, and improves the built-in field, thus explaining the observed gains in Voc, FF, and the elimination of rollover in thicker devices. The combination of ultra-thin absorbers, high carrier concentration, and strong intrinsic absorption allows the depletion region to remain confined while still ensuring effective photogeneration and collection. This thickness regime, assisted by controlled oxygen incorporation during PAT, mitigates the usual drawbacks of full depletion in thin absorbers and enables efficient devices with only 400 nm of Sb_2Se_3. Accelerated aging tests up to 200 h at 80 °C and one-sun illumination show that all devices remain stable, with a slight performance improvement in PAT-treated cells, further supporting the beneficial and durable nature of oxygen-induced defect passivation.

CRediT authorship contribution statement

N. Torabi: Writing – original draft, Investigation, Data curation. **J. M. Delgado-Sanchez:** Investigation, Data curation. **E. Artegiani:** Writing – review & editing, Supervision, Investigation, Data curation. **J. Kuliček:** Investigation, Data curation. **B. Rezek:** Validation, Formal analysis, Data curation. **P. Jakuza:** Investigation. **M. Meneghini:** Supervision. **A. Romeo:** Writing – review & editing, Validation, Supervision, Project administration, Investigation, Funding acquisition, Data curation, Conceptualization.

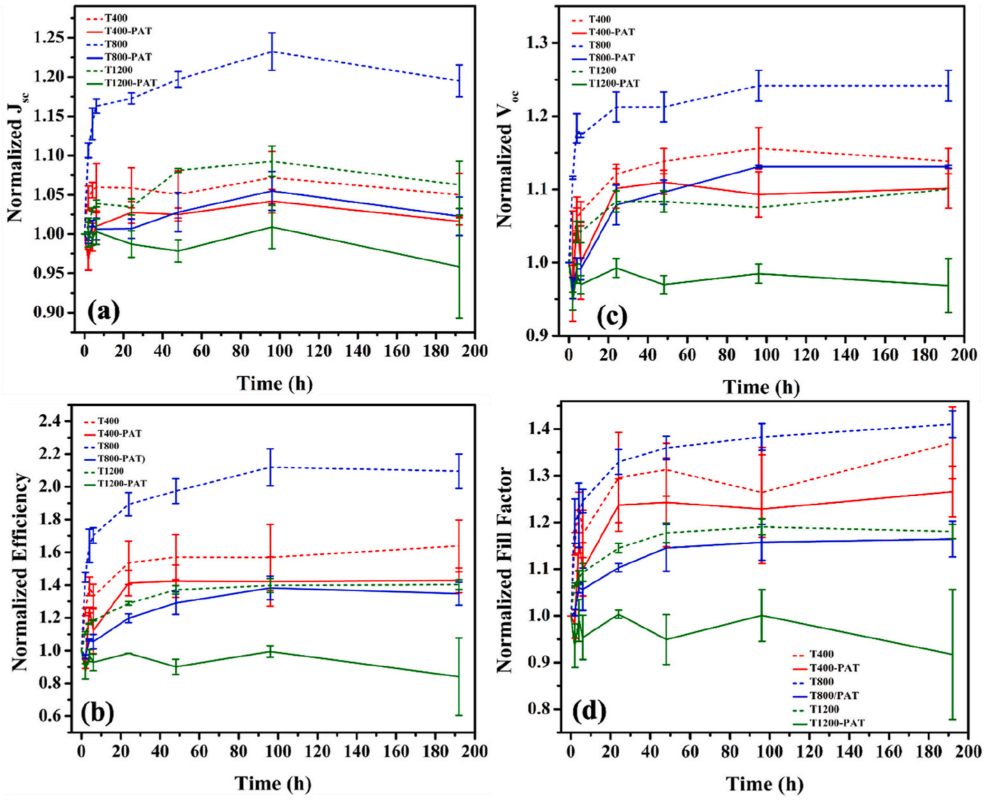

Fig. 11. Photovoltaic parameters degradation over time under accelerated stability test of various thick Sb_2Se_3 solar cells before and after PAT.

Open data

The data related to the manuscript are available upon request from the authors or online from the Zenodo repository: https://doi.org/10.5281/zenodo.15429859.

Declaration of competing interest

The authors declare that they have no known competing financial interests or personal relationships that could have appeared to influence the work reported in this paper.

Acknowledgments

This article is based upon the work from COST Action ReNewPV CA21148, supported by COST (European Cooperation in Science and Technology). The research work has been supported by the ACT-FAST project, n. CETP22_00039 within CET-partnership program. The Italian Ministry of Education is thankfully acknowledged. Fondazione Cariverona has partially supported this work within the INSOBILD project, n. 52271.

B.R. and J.K. are thankful for the support of the Ministry of Education, Youth, and Sports (MEYS) with project No. CZ.02.01.01/00/22_008/0004617 (EcoStor) under the Operational Programme Johannes Amos Comenius.

Appendix A. Supplementary data

Supplementary data to this article can be found online at https://doi.org/10.1016/j.mssp.2026.110428.

Data availability

Data will be made available on request.

References

[1] A. Mavlonov, et al., A review of Sb2Se3 photovoltaic absorber materials and thin-film solar cells, Sol. Energy 201 (May 2020) 227–246, https://doi.org/10.1016/J.SOLENER.2020.03.009.

[2] F. Kosek, J. Tulka, L. Štourač, Optical, photoelectric and electric properties of single-crystalline Sb2Se3, Czech. J. Phys. B 28 (3) (Mar. 1978) 325–330, https://doi.org/10.1007/BF01597220, 1978 28:3.

[3] Y. Zhou, et al., Thin-film Sb2Se3 photovoltaics with oriented one-dimensional ribbons and benign grain boundaries, Nat. Photonics 9 (6) (May 2015) 409–415, https://doi.org/10.1038/nphoton.2015.78, 2015 9:6.

[4] Z. Duan, et al., Sb2Se3 thin-film solar cells exceeding 10% power conversion efficiency enabled by injection vapor deposition technology, Adv. Mater. 34 (30) (Jul. 2022) 2202969, https://doi.org/10.1002/ADMA.202202969.

[5] Y. Zhao, et al., Regulating deposition kinetics via a novel additive-assisted chemical bath deposition technology enables fabrication of 10.57%-efficiency Sb2Se3 solar cells, Energy Environ. Sci. 15 (12) (Oct. 2022) 5118–5128, https://doi.org/10.1039/d2ee02261c.

[6] Z.-X. Cao et al., "Thickness-Dependent Carriers Transport in Sb 2 Se 3 Thin Film Solar Cells", doi: 10.1007/s12598.

[7] J. Zhao, et al., Unveiling the influence of absorber thickness on efficient Sb2(S, Se) 3 solar cells through controlled chemical Bath deposition, Surf. Interfaces 42 (Nov) (2023), https://doi.org/10.1016/j.surfin.2023.103411.

[8] M. Mukhtar, et al., How the selenium is affecting the physical and electrical properties of ultra-thin CdSeTe/CdTe solar cells, Sol. Energy Mater. Sol. Cell. 293 (Dec) (2025), https://doi.org/10.1016/j.solmat.2025.113830.

[9] A. Salavei, I. Rimmaudo, F. Piccinelli, A. Romeo, Influence of CdTe thickness on structural and electrical properties of CdTe/CdS solar cells, Thin Solid Films 535 (May 2013) 257–260, https://doi.org/10.1016/j.tsf.2012.11.121.

[10] X. Hu, et al., Improving the efficiency of Sb2Se3 thin-film solar cells by post annealing treatment in vacuum condition, Sol. Energy Mater. Sol. Cell. 187 (Dec. 2018) 170–175, https://doi.org/10.1016/J.SOLMAT.2018.08.006.

[11] R. Tang, et al., Highly efficient and stable planar heterojunction solar cell based on sputtered and post-selenized Sb2Se3 thin film, Nano Energy 64 (Oct. 2019) 103929, https://doi.org/10.1016/J.NANOEN.2019.103929.

[12] S. Yao, et al., Improved performance of thermally evaporated Sb2Se3 thin-film solar cells via substrate-cooling-speed control and hydrogen-sulfide treatment, ACS Appl. Mater. Interfaces 12 (21) (May 2020) 24112–24124, https://doi.org/10.1021/ACSAMI.0C03674.

[13] Y. Li, et al., Atomic-scale defect reconfiguration via thermally induced structural ordering for high-efficiency Sb2Se3Solar cells, ACS Nano 19 (37) (Sep. 2025) 33460–33472, https://doi.org/10.1021/acsnano.5c10733.

[14] N. Fleck, et al., How oxygen exposure improves the back contact and performance of antimony selenide solar cells, ACS Appl. Mater. Interfaces 12 (47) (Nov. 2020) 52595–52602, https://doi.org/10.1021/ACSAMI.0C14256.

[15] D. Ren, et al., Study of Sb2Se3/Al interface affected by oxygen exposure, Vacuum 215 (2023), https://doi.org/10.1016/j.vacuum.2023.112393.

[16] N. Torabi, et al., Analysis of CdSe as an alternative buffer layer for Sb2Se3 solar cells, Sol. Energy 264 (2023), https://doi.org/10.1016/j.solener.2023.111990.

[17] C. Zhang, et al., Mechanism of defect passivation in Sb2Se3 solar cells via buried selenium seed layer, Adv. Energy Mater. 15 (7) (Feb. 2025), https://doi.org/10.1002/aenm.202403352.

[18] N. Torabi, et al., Analysis of CdSe as an alternative buffer layer for Sb2Se3 solar cells, Sol. Energy 264 (Nov) (2023), https://doi.org/10.1016/j.solener.2023.111990.

[19] J.T. Heath, J.D. Cohen, W.N. Shafarman, Bulk and metastable defects in CuIn1-xGaxSe2 thin films using drive-level capacitance profiling, J. Appl. Phys. 95 (3) (2004) 1000–1010, https://doi.org/10.1063/1.1633982.

[20] X. Wang, S.R. Kavanagh, D.O. Scanlon, A. Walsh, Upper efficiency limit of Sb2Se3 solar cells, Joule 8 (7) (Jul. 2024) 2105–2122, https://doi.org/10.1016/j.joule.2024.05.004.